Residual bubble volume formed behind a sphere plunging into liquid bath (meniscus breakdown with finite velocity of sphere penetration)

Residual bubble volume formed behind a sphere plunging into liquid bath (meniscus breakdown with finite velocity of sphere penetration)

Kenji Katoh, Tatsuro Wakimoto, Yoshiaki Ueda, Manabu Iguchi

KATOH K., WAKIMOTO T., IGUCHI M., & UEDA Y. (2018). Residual bubble volume formed behind a sphere plunging into liquid bath (meniscus breakdown with finite velocity of sphere penetration). Physics of Fluids. 30. 082106. DOI: 10.1063/1.5040315

Residual bubble volume formed behind a sphere plunging into liquid bath (meniscus breakdown with finite velocity of sphere penetration)

Kenji Katoh, Tatsuro Wakimoto, Yoshiaki Ueda, and Manabu Iguchi

Citation: Physics of Fluids **30**, 082106 (2018); doi: 10.1063/1.5040315
View online: https://doi.org/10.1063/1.5040315
View Table of Contents: http://aip.scitation.org/toc/phf/30/8
Published by the American Institute of Physics

Residual bubble volume formed behind a sphere plunging into liquid bath (meniscus breakdown with finite velocity of sphere penetration)

Kenji Katoh,[1,a)] Tatsuro Wakimoto,[1] Yoshiaki Ueda,[2] and Manabu Iguchi[1]
[1]*Department of Mechanical Engineering, Osaka City University, 3-3-138 Sugimoto Sumiyoshi-ku, Osaka 558-8585, Japan*
[2]*Department of Mechanical Engineering, Setsunan University, 17-8, Ikedanakamachi, Neyagawa 572-8508, Japan*

(Received 16 May 2018; accepted 19 July 2018; published online 7 August 2018)

The residual bubble formed from spherical particles plunging into a liquid bath has an important effect on the performance of CaO particles used for the desulfurization of melted iron. Previous work has theoretically estimated the residual bubble volume resulting from quasi-static sphere immersion by applying the energy minimization principle to the gas–liquid interface meniscus at its rupture [Katoh *et al.*, "Residual bubble formed behind a sphere plunging into liquid bath (in Japanese)," Jpn. J. Multiphase Flow **28**, 547–553 (2015)]. Here, we propose a method to theoretically estimate the residual bubble volume for sphere penetration with a finite velocity from 0.05 to 30 mm/s into a liquid bath. To do so, the meniscus rupture at the sphere's critical depth was calculated via a dynamic equation in which the energy gradient along the sphere surface was considered as the driving force to move the triple-phase contact line. The bubble volume was then estimated by calculating the system energy at the meniscus breakpoint and by using the principle of minimum energy. The model results were verified experimentally for a variety of liquids, showing that the proposed model can be used for estimation of the residual bubble volume. *Published by AIP Publishing.* https://doi.org/10.1063/1.5040315

I. INTRODUCTION

The behavior of the gas–liquid interface formed above spherical particles plunging into a liquid is an important phenomenon for various engineering fields. Pioneering studies of solid–liquid impact include the studies of Worthington and Cole[2] and Worthington and Cole,[3] who used single-spark photography to examine the splash and air cavity shapes formed by the vertical entry of a sphere into water. In the mid-1900s, the studies of the water-entry problem of a sphere were prompted by military applications.[4–8] Recently, high-speed photography has been used to show the instantaneous nature of cavity growth and closure and to observe the movement of the sphere.[9–15] Duclaux *et al.*[9] experimentally observed the temporal variation of the cavity shape and compared it with the approximate analytical one derived by extending the method used to solve the classical Besant–Rayleigh problem. Aristoff and Bush[10] extended this work by including the effects of surface tension and aerodynamic pressure on the cavity surface, as well as the influence of sphere deceleration on the resulting cavity shape. Truscott *et al.*[11] estimated unsteady forces acting on the sphere from the trajectory of the sphere. Several investigations have shown the influence of the wettability of the sphere surface on the phenomenon. Duez *et al.*[12] demonstrated that a hydrophilic sphere requires a larger impact velocity than a hydrophobic sphere to produce the air cavity. Tanaka *et al.*,[13] Tanaka *et al.*,[14] and Ueda *et al.*[15] also revealed that the air cavity on a hydrophobic sphere grows more rapidly even at low impact velocities. The equation of motion of a hydrophobic sphere entering into water was derived by Lee and Kim,[16] and numerical approaches have been able to reproduce the cavity.[17–19] The air cavity and movement of entering objects had also been investigated for deformable sphere[20] and aspherical objects.[21,22] These studies have advanced scientific knowledge on the behavior of an air cavity formed on an object as it enters a liquid bath. Truscott *et al.*[22] reviewed the subjects in this field.

It is also important to understand the behavior of the residual bubble attached to a sphere after the cavity collapses or the meniscus representing the gas–liquid interface breaks (pinch-off in the quasi-static seal regime). Observation with high speed imaging and numerical simulation of a sphere plunging into a liquid bath have revealed that a bubble attaches to the sphere after the cavity or the meniscus breaks.[18,23,24] In the steel smelting process, the poor wettability of CaO particles used as a desulfurizing agent with molten pig iron causes residual air bubbles on the surface of the particles after the meniscus breaks. The adhesion of these air bubbles can have adverse effects on the process, including increasing particle drag and inhibiting chemical reactions. Studies have identified the need to accurately estimate the volume of bubbles adhering to particles to evaluate the performance of engineering devices.[14,25] However, although work has been performed addressing the behavior of the gas–liquid interface around the solid spheres plunging into a liquid,[9–12] little work has been performed to accurately estimate the volume of the residual bubble adhering to the spherical particle.

The purpose of this study is to investigate the behavior of the triple-phase contact line on a sphere plunging into a liquid

[a)]Author to whom correspondence should be addressed: katoh@mech.eng.osaka-cu.ac.jp. Telephone: +81-6-6605-2665. Fax: +81-6-6605-2953.

and to estimate the volume of the bubble remaining attached to the sphere after the meniscus breaks. Previous work has proposed a theoretical model as a first step to obtain the bubble volume for the quasi-static penetration of a spherical particle.[1] Applying the principle of minimum energy of the system, geometrical parameters determining the gas-liquid interfacial meniscus shape at its rupture were obtained, and the bubble volume attached to the sphere was calculated from the volume surrounding the gas–liquid interface and the sphere surface. The model results showed a good agreement with experimental bubble volumes for two kinds of spherical particles having different wettability.

In this study, a theoretical model is proposed to estimate the bubble volume for the penetration of a particle with a finite velocity. An equation of motion was used to describe the behavior of the triple-phase contact line while the particle enters into the liquid with a finite velocity. The gradient of the system energy with respect to the contact line movement was considered as the force driving the bulk liquid motion until the meniscus breaks. From the solution of the equation, we estimated the critical depth of the sphere at the point of meniscus rupture. The bubble volume was then calculated using the energy minimization principle for the gas–liquid interface profile when the meniscus breaks at the critical depth from the static liquid surface. Experimental trials were run to validate the proposed model. There, we measured the time of meniscus rupture and the residual bubble volume on spherical particles with relatively low penetration speeds (U = 0.05–30 mm/s) with different wettability. The validity of the proposed theoretical model was verified from the comparison of the time of meniscus rupture and of the bubble volume with the experimental results. The influence of wettability, sphere radius, and liquid property on the volume of the bubble adhering to the sphere was considered.

II. EXPERIMENTAL METHOD

The experimental setup used in this study is schematically shown in Fig. 1. A sphere of stainless steel (SUS304) (radius R_S = 2, 4, and 6.35 mm) was fixed in an acrylic vessel ④ with a supporting rod ③ attached to the bottom of the sphere. The test liquid was then poured from the upper tank ⑨ to raise the liquid level at the speed set by the valve ⑥. The velocity of sphere penetration U was changed within U = 0.05–30 mm/s in this experiment. Although we used a supporting rod with a diameter of 4 mm, which is comparable to the sphere diameter, for ensuring adequate rigidity, any influence of the wake behind the rod on the axisymmetric contact line and the liquid surface was not observed. Tap water, 20% aqueous ethanol, and 60% aqueous glycerol were used as the test liquids. Their surface tension (σ), density (ρ), and kinematic viscosity (ν) were measured by the Wilhelmy method, Baumé's hydrometer, and Ubbelohde viscometer, respectively; their physical properties are shown in Table I.

Two types of water repellents, FS-1060TH-0.5 (Fluoro Technology Co.) (Repellent 1) and HIREC 1450NF (NTT Advanced Technology Co.) (Repellent 2), were used to vary the wettability between the test liquid and the sphere. Because the solid sphere entered the liquid, it was necessary to consider

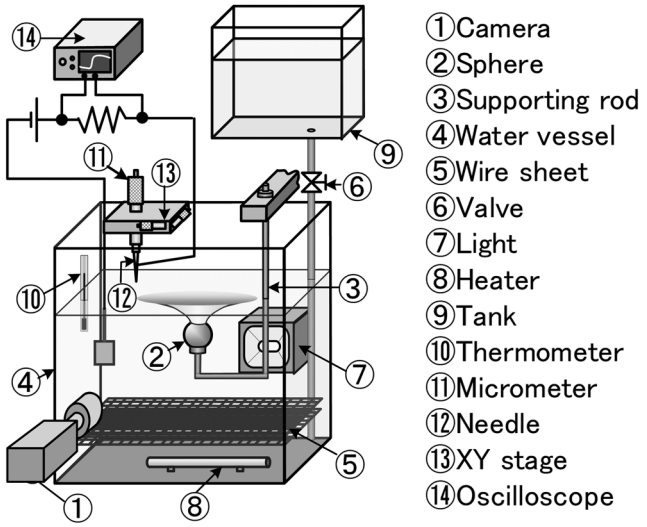

FIG. 1. Schematic of the experimental apparatus.

TABLE I. Properties of test liquids.

	σ (mN/m)	ρ (kg/m^3)	ν (mm^2/s)
Water (10 ± 1 °C)	73.8 ± 0.3	1000 ± 1	1.32 ± 0.03
Ethanol 20% (20 ± 1 °C)	39.1 ± 0.2	970 ± 1	2.21 ± 0.04
Glycerol 60% (20 ± 1 °C)	68.7 ± 0.3	1158 ± 1	10.15 ± 0.1

the advancing contact angle as an index of wettability.[26] To measure the advancing contact angle while avoiding the effect of dynamic wetting, the sphere coated with a water repellent was fixed in vessel ④ while raising the liquid levels at a speed less than 1 mm/min. The photographs of the gas–liquid interface near the contact line were taken to generate a polynomial to approximate the interface profile. The advancing contact angle θ_A was then determined from the gradient of the polynomial at the contact line. This process was repeated over six times for each combination of the liquid and water-repellent spray chosen. Average results of θ_A are shown in Table II. The contact angle of Repellent 1 was found to be less than 100° for ethanol and glycerol aqueous solutions, and thus, the volume of attached bubbles was extremely small. Thus, only Repellent 2 was used for these solutions. Furthermore, a relatively high deviation of contact angles was measured for Repellent 2. These could be caused by the roughness observed on the surface of the sphere due to the fine particles, several micrometers in diameter that were mixed in Repellent 2.

The movement of the triple-phase contact line on the surface of the sphere was tracked by using a high-speed video camera. A schematic diagram showing the change in the meniscus (gas–liquid interface) shape attached to a sphere penetrating into a liquid with velocity U and the resulting behavior

TABLE II. Advancing contact angles θ_A.

	Repellent 1 (deg)	Repellent 2 (deg)
Water	118 ± 2	155 ± 5
Ethanol 20%	–	100 ± 2
Glycerol 60%	–	136 ± 3

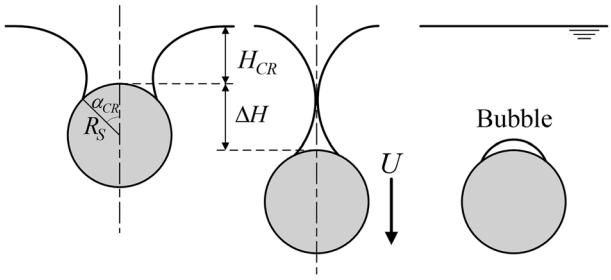

FIG. 2. Behavior of the axisymmetric meniscus on the sphere.

of the triple-phase contact line is displayed in Fig. 2. In the case of quasi-static penetration, the shape of the meniscus that adheres to the sphere is determined from the axisymmetric Laplace equation shown in Eq. (1), which represents the force balance at the gas–liquid interface,[27]

$$\sigma\left[-\frac{d^2z/dr^2}{\left\{1+(dz/dr)^2\right\}^{3/2}}-\frac{|dz/dr|}{r\sqrt{1+(dz/dr)^2}}\right]=-\rho gz. \quad (1)$$

Here, r and z represent the coordinates in the radial direction and the vertical direction, respectively, and g is the gravitational acceleration. $z = 0$ corresponds to the stationary liquid surface. As the depth of the top of the sphere H from the stationary liquid surface is increased quasi-statically, there is a critical depth H_{CR} at which the given Laplace equation has no solution satisfying the condition that the meniscus attaches to the sphere with the advancing contact angle θ_A. When the sphere reaches the critical depth during quasi-static penetration, the system becomes unstable, and the contact line begins to move along the sphere surface toward its head. When the sides of the meniscus curve come in contact with each other near the sphere head, the residual bubble is formed at H_{CR}.

In the case of penetration with a finite velocity, the influence of the inertial force can be estimated by the Weber number, *We*,

$$We=\frac{\rho U^2 R_S}{\sigma}. \quad (2)$$

Considering the conditions used in this study (U = 0.05–30 mm/s and R_S = 2–6.35 mm), the Weber number defined by Eq. (2) is at most $We \sim 0.1$. As a result, the shape of the gas–liquid interface may still be approximated by the solution of static Laplace equation given in Eq. (1). During penetration with a finite velocity, the meniscus becomes unstable near H_{CR}. However, the sphere continues to sink after reaching the critical depth, and the bubble is formed at a deeper position, $H_{CR} + \Delta H$, as shown in Fig. 2. For the purposes of this study and to propose a simple theoretical model, the bubble volume for the finite velocity will be determined in Sec. III by considering the model in which the effect of U is superimposed on the basis of quasi-static particle penetration. Thus, the reference time $t = 0$ was designated as the moment when the sphere depth reaches H_{CR} for the quasi-static penetration. When the sphere reaches $H = H_{CR}$, the observation was started to measure the trajectory of the triple-phase contact line up to the rupture of the meniscus.

To observe the motion of the contact line, the needle probe ⑫ was attached to the micrometer head ⑪ and was set at height H_{CR} from the top of the sphere, as shown in Fig. 1. The probe was then horizontally moved by the XY stage ⑬ to a position sufficiently far from the sphere. Since voltage was impressed between the needle and the liquid, the instance when the stationary liquid level reaches the height H_{CR} can be recognized with the signal on the oscilloscope. The liquid level is raised, and high-speed video recording begins using the camera ① [Keyence, VW-9000, Image size: 640 × 480 (pixel^2)] when the liquid surface touches the needle, thus allowing the movement of the contact line on the sphere surface from $t = 0$ to be observed. Figure 3 shows the sequential photographs of the movement of the contact line on the sphere surface. When the sphere reaches H_{CR} at $t = 0$, as shown in Fig. 3(a), the contact line moves on the surface of the sphere with a velocity corresponding to that of sphere penetration. Then, the speed of movement of the contact line is accelerated gradually, and finally, the meniscus breaks at t = 26.8 ms, as shown in Fig. 3(e). Note that an ellipse is drawn in Fig. 3(e) for comparison. The details will be stated in Sec. III. From the obtained images, as in Fig. 3, we measured the change in the position of

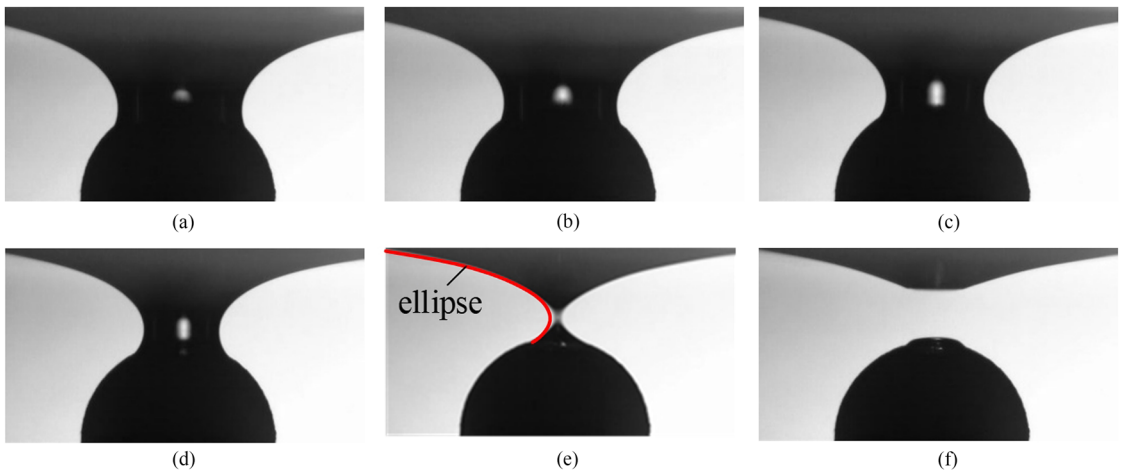

FIG. 3. Sequence photographs for the movement of contact line (water, θ_A = 155°, *Rs* = 2 mm, U = 10 mm/s). (a) t = 0, (b) t = 7 ms, (c) t = 14 ms, (d) t = 21 ms, (e) t = 26.8 ms, and (f) residual bubble.

the contact line with time and the time T at which the meniscus broke and the residual bubble was formed on the sphere. We retook a high-resolution image of the residual bubble with a digital still camera [Nikon D70S, image size: 3008 × 2000 (pixel^2)] and calculated the bubble volume in the image by integrating the volume surrounded by the axisymmetric gas–liquid interface and the sphere wall. The accuracy of this volume measurement was estimated to be 1.6%–8.7% based on the spatial resolution of the image (=1.8–5.7 μm/pixel). The average of three trials of each liquid and sphere combination was used as the experimental result. The scatter of the break time and bubble volume was within ±10% for the trailed experimental conditions.

III. THEORETICAL CONSIDERATION

With T defined as the time when the meniscus breaks, the residual bubble is formed at $\Delta H = UT$ deeper than H_{CR}, as shown in Fig. 2. In this study, we calculated the bubble volume using the same principle of minimum energy as in the quasi-static penetration stated in the preceding report[1] at the position $H = H_{CR} + UT$ using a dynamic model to theoretically obtain the time T. In Sec. III A, first we briefly touch the method of energy minimization to estimate the bubble volume for the quasi-static sphere penetration. Then the dynamics of meniscus up to its rupture as shown in Fig. 3 will be discussed in Sec. III B.

A. Residual bubble volume in quasi-static penetration

A schematic view immediately before the meniscus breaks is presented in Fig. 4. Here, H is the sphere depth, and $H = H_{CR}$ for quasi-static penetration, and $H = H_{CR} + UT$ for penetration with a finite velocity. In the figure, α represents the angle at the sphere center from the contact line position to the sphere top, β indicates the angle between the horizontal line and the line segment connecting the contact line position and the center of the circular gas–liquid interface with radius R, and θ represents the contact angle observed when the meniscus breaks. If the gas–liquid interface of the meniscus shape

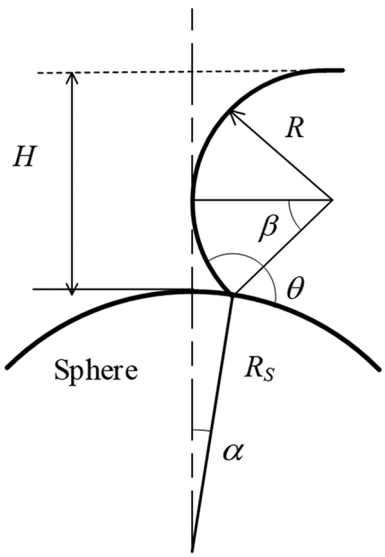

FIG. 4. Schematic of residual bubble generation.

is approximated by a simple circular arc of radius R, as shown in Fig. 4, the relations from geometrical conditions for angles β, α, and R can be written as Eqs. (3) and (4),

$$R(1 + \sin\beta) = H_{CR} + R_S(1 - \cos\alpha), \tag{3}$$

$$R(1 - \cos\beta) = R_S \sin\alpha. \tag{4}$$

The center angle α of the contact line position is determined from the minimum energy condition, and β and R can then be determined from Eqs. (3) and (4) from the obtained α. Thus we can calculate the bubble volume V as that surrounded by the gas–liquid interface and sphere wall, as shown in Fig. 4,

$$V = \pi R^3\left(\frac{1}{12}\sin 3\beta - \frac{1}{2}\sin 2\beta + \frac{7}{4}\sin\beta - \beta\right) - \pi {R_S}^3\left(\frac{1}{3}\cos^3\alpha - \cos\alpha + \frac{2}{3}\right). \tag{5}$$

The overall system energy can be considered as a summation of its three parts: the surface energy E_S of the gas–liquid interface, the liquid potential energy E_P, and the energy E_W due to the wetting behavior of the contact line. The reference energy was defined as that for the stationary liquid surface and the wetted sphere.

E_S can be obtained by multiplying the surface tension σ by the difference of surface area between the meniscus and the surface of the stationary liquid. A geometrical consideration allows for E_S to be expressed as Eq. (6),

$$E_S = 2\pi R^2\sigma\left(\frac{\pi}{2} + \beta - 1 - \sin\beta\right) - \pi R^2\sigma. \tag{6}$$

E_P of the liquid can be calculated from the energy increment of the liquid displaced by the air cavity, shown in Eq. (7),

$$E_P = \rho g\pi R^4\left[\frac{5}{3} - \frac{\pi}{2} + 2\sin\beta - \frac{1}{3}\sin^3\beta - \frac{1}{2}\sin 2\beta - \beta - \frac{1}{4}\cos^4\beta + \frac{2}{3}\cos^3\beta - \frac{1}{2}\cos^2\beta\right] - \rho g\pi {R_S}^3 \times\left[(H_{CR} + R_S)\left(\frac{1}{3}\cos^3\alpha - \cos\alpha + \frac{2}{3}\right) - \frac{1}{4}R_S\sin^4\alpha\right]. \tag{7}$$

Please refer to the Appendix for details about the derivations of Eqs. (5)–(7).

E_W, related to the wetting behavior of the contact line, can be found by multiplying the wetted area of the immersed sphere by the energy difference per unit area between the solid surface and the solid–liquid interface. By applying the advancing contact angle to Young's equation, E_W can be obtained as shown in Eq. (8),[26]

$$E_W = 2\pi\sigma {R_S}^2\cos\theta_A(1 - \cos\alpha). \tag{8}$$

The system energy E can then be obtained from the sum of three energies E_S, E_P, and E_W calculated from Eqs. (6)–(8).

After the meniscus becomes unstable, the contact line advances on the spherical surface. When the meniscus breaks, the contact angle $\theta \geqq \theta_A$ can be observed because of the dynamic wetting effect.[28,29] We then obtained $\alpha_{\min}$, where the system energy E takes the minimum value under the condition of $\theta \geqq \theta_A$ using Eq. (9),

$$E(\alpha_{\min}) = \mathrm{Min}[E(\alpha)|\theta \geq \theta_A]. \quad (9)$$

Using the above $\alpha_{\min}$, the volume of residual bubble was determined from Eq. (5) by using Eqs. (3) and (4).

The above results were obtained based on the circular meniscus profile shown in Fig. 4. As shown in Fig. 3(e), the actual meniscus shape looks noticeably different from a circular arc. However, because the system energy is estimated by integrating over the meniscus profile assuming the satisfaction of appropriate boundary conditions, it could be rather insensitive to the accuracy of approximation.[30] As a trial, we calculated the bubble volume from the same energy minimization when the meniscus shape was approximated by an ellipse. For example, an ellipse with a semi-major axis of 8 mm was assumed, and the other parameters, such as a semi-minor axis or contact line position, were determined from energy minimization and geometrical conditions. The resulting profile of the ellipse is drawn in Fig. 3(e). The ellipse well approximates the actual meniscus profile.

Figure 5 shows a comparison of the volume of the experimental bubble[1] with the volumes determined theoretically by using a circle and an ellipse. As shown in the figure, the bubble volume does not significantly depend on the approximation to the meniscus profile. The experimental values of the two tested contact angles showed good agreement with both theoretical curves. In this study, to calculate the bubble volume as simply as possible, we calculate the system energy by assuming a circular arc as the meniscus curve in Sec. III B in the scenario that the sphere is plunging into a liquid with a finite velocity.

B. Bubble volume at finite penetration velocity

An equation of motion based on the energy change in the system with the movement of the contact line is then proposed to estimate the time when the meniscus breaks. Because the influence of inertia is not significant in this experiment, it is possible to approximately obtain the system energy from Eq. (1). An example of the energy change with respect to the contact line position in the coordinate s direction along the sphere's surface is presented in Fig. 6, where $s = 0$ in the abscissa indicates the contact line position at $t = 0$ when the advancing contact angle θ_A appears. E_{CR} refers to the system energy at $s = 0$. In the figure, the calculated results are shown for the critical depth $H = H_{CR}$ as well as for a slightly shallow position, that is, $H = H_{CR}$−0.2 mm. The coordinates of the top of the sphere can be expressed as $s = R_s\alpha_{CR}$, where α_{CR} indicates the central angle of the initial contact line at $t = 0$. This geometric relationship is shown in Fig. 7. The system energy at each position $s = R_s\alpha$ can be obtained from the solution of the Laplace equation (1) with the boundary conditions as follows:

$$r = R_S \sin\alpha : z = H_{CR} - R_S(1 - \cos\alpha),$$
$$r \to \infty : \frac{dz}{dr} \to 0. \quad (10)$$

The energy $E(s)$ can be obtained from the sum of the energy of the gas–liquid interface, potential energy, and work of wetting, as shown in Eq. (11),

$$E(s) = \int_{R_S \sin\alpha}^{\infty} \left[2\pi r\sigma \left\{ \sqrt{1 + \left(\frac{dz}{dr}\right)^2} - 1 \right\} + \rho g \left\{ \pi r^2 z \frac{dz}{dr} \right\} \right] dr$$
$$+ 2\pi {R_S}^2 \sigma \cos\theta_A (1 - \cos\alpha). \quad (11)$$

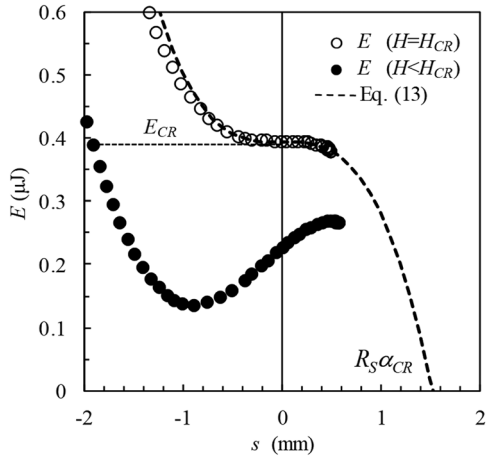

FIG. 6. System energy distribution dependent on the contact line position (water, R_S = 4 mm. θ_A = 118°).

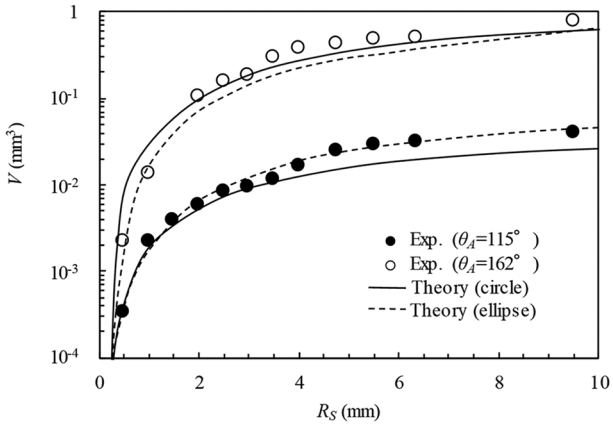

FIG. 5. Comparison of the residual bubble volumes between the experimental results and the theoretical model.

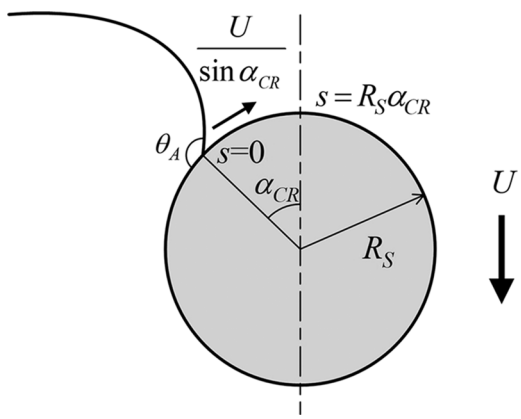

FIG. 7. Geometrical relation of the meniscus attached to the sphere.

By using the numerical solution of Eq. (1) obtained by the Runge–Kutta method, the above energy was calculated. Note that the calculation results obtained using Eq. (11) are plotted in Fig. 6; these results were obtained until the Laplace equation (1) did not have any solution satisfying the boundary conditions of Eq. (10). As shown in the figure, when the depth is smaller than H_{CR}, the system is stable at the contact line position with minimum energy, that is, $dE/ds = 0$. On the other hand, when the sphere reaches the critical depth $H = H_{CR}$ at $t = 0$, the system becomes neutral stable, i.e., $d^2E/ds^2 = 0$ at $s = 0$. The energy monotonously decreases with respect to the displacement of the contact line toward the top of the sphere, as shown in Fig. 6. The meniscus then contracts and breaks near the top of the sphere. Because the bubble size formed after the meniscus breaks is sufficiently small compared with the sphere radius R_S, we may assume that the system energy E at the break is quite smaller than E_{CR}. Thus, the relations shown in Eq. (12) may be drawn for the energy $E(s)$ at $s = 0$ and $s = R_S\alpha_{CR}$,

$$\begin{aligned} &s = 0 : E = E_{CR}, \quad \frac{dE}{ds} = 0, \quad \frac{d^2E}{ds^2} = 0, \\ &s = R_S\alpha_{CR} : E \approx 0. \end{aligned} \tag{12}$$

For the sake of simplicity, the energy change $E(s)$ with respect to the movement of the contact line was approximated by a third-order polynomial satisfying the condition of Eq. (12), as shown in Eq. (13),

$$E = E_{CR}\left[1 - \left(\frac{s}{R_S\alpha_{CR}}\right)^3\right]. \tag{13}$$

Equation (13) is also drawn in Fig. 6 for the purpose of comparison. As shown in the figure, Eq. (13) can approximate the energy distribution around $s = 0$. The energy distribution of Eq. (13) may be applied to the contact line position s as well in the event that there is no solution of the Laplace equation.

If we recognize that the energy gradient $(-dE/ds)$ of Eq. (13) corresponds to the force which drives the movement of the contact line, the following relation can be written as the equation of motion for the position $s(t)$ of the contact line after the meniscus becomes unstable at $t = 0$:

$$-\left(\frac{dE}{ds}\right) = \rho V_L a. \tag{14}$$

Here, V_L represents the approximate volume of the liquid moving with the contact line, and a is the acceleration of contact line movement ($a \equiv d^2s/dt^2$). To roughly obtain the rupture time of meniscus, V_L was approximated by Eq. (15), which roughly corresponds to the volume of the initial air cavity that would be filled by the liquid. The volume was simply approximated by a cylinder with a radius equal to the distance between the position of attachment of the contact line ($\sim R_S\alpha_{CR}$) and the height of the meniscus (H_{CR}) as follows:

$$V_L \sim \pi(R_S\alpha_{CR})^2 H_{CR}. \tag{15}$$

Combining Eqs. (13)–(15), the acceleration a of the contact line can be obtained,

$$a = \frac{3E_{CR}}{\rho V_L R_S\alpha_{CR}}\left(\frac{s}{R_S\alpha_{CR}}\right)^2. \tag{16}$$

Furthermore, the relation shown in Eq. (17) between the acceleration and the contact line velocity ($v \equiv ds/dt$) can then be written,

$$\frac{dv}{dt} = \frac{dv}{ds} \times \frac{ds}{dt} = \frac{d}{ds}\left(\frac{1}{2}v^2\right) = a. \tag{17}$$

v can then be obtained from Eqs. (16) and (17) as follows:

$$v = \sqrt{\frac{2E_{CR}}{\rho V_L}}\sqrt{\left(\frac{s}{R_S\alpha_{CR}}\right)^3 + C}. \tag{18}$$

Setting $v = v_0$ at $s = 0$, v can then be determined,

$$\bar{v} = \sqrt{\bar{s}^3 + \bar{v}_0^2}, \tag{19}$$

where $\bar{v}$ and $\bar{s}$ indicate the non-dimensional values defined by the following expressions:

$$\bar{v} = \frac{v}{\sqrt{2E_{CR}/\rho V_L}}, \quad \bar{s} = \frac{s}{R_S\alpha_{CR}}. \tag{20}$$

The initial velocity v_0 can be approximated as the circumferential velocity of the contact line corresponding to the penetration velocity U of the sphere as

$$v_0 = \frac{U}{\sin\,\alpha_{CR}}. \tag{21}$$

It was confirmed through experimental observation at $H = H_{CR}$ that the velocity can be approximated by Eq. (21). Because the driving force $(-dE/ds)$ due to the energy gradient should be zero at the critical depth, the tangential velocity may be simply approximated by Eq. (21) corresponding to the sphere penetration.

From the relationship between v and s, the following expression can be written:

$$\begin{aligned} &\frac{d\bar{s}}{d\bar{t}} = \bar{v}\left(\bar{t} \equiv \sqrt{\frac{2E_{CR}}{\rho V_L}}\frac{t}{R_S\alpha_{CR}}\right), \\ &\therefore \frac{d\bar{s}}{\bar{v}} = d\bar{t} = \frac{d\bar{s}}{\sqrt{\bar{s}^3 + \bar{v}_0^2}}. \end{aligned} \tag{22}$$

From Eq. (22), the trajectory of contact line movement $s(t)$ can then be obtained using Eq. (23),

$$\bar{t} = \int_0^{\bar{s}} \frac{d\bar{s}}{\sqrt{\bar{s}^3 + \bar{v}_0^2}}. \tag{23}$$

The rupture time of the meniscus, T, can then be obtained by numerically integrating Eq. (24),

$$\bar{T} = \int_0^1 \frac{d\bar{s}}{\sqrt{\bar{s}^3 + \bar{v}_0^2}}. \tag{24}$$

In the above analysis, we assumed that the system energy at the meniscus break is approximated as $E \approx 0$ in Eqs. (12) and (13). In addition, the meniscus actually breaks somewhere before $s = R_S\alpha_{CR}$, as described in Eq. (12). The calculated results in Sec. IV show that the actual energy at the meniscus break is about 20% of E_{CR} in the experimental conditions treated here. Assuming $E = 0.2E_{CR}$ at $s = 0.9R_S\alpha_{CR}$ in

Eqs. (12) and (13), the deviation of T was estimated by using Eq. (24). The results show that the difference is less than 6% from the value using $E = 0$. Since the contact line speed is quickly accelerated with the steep energy gradient, as shown in Fig. 6, and becomes sufficiently large when the meniscus breaks, we can safely neglect the influence of deviation in the boundary conditions stated above to estimate the rupture time T.

Using the results of T, the bubble volume was obtained from the principle of minimum energy in Sec. III A at the sphere depth of $(H_{CR} + UT)$.

IV. EXPERIMENTAL RESULTS AND DISCUSSION

A. Trajectory of the contact line and rupture time of the meniscus

Examples of contact line trajectories using the theoretical model compared with the experimental results are shown in Fig. 8. When the penetration speed U was relatively small, the theoretical results drawn by the solid and broken lines roughly agree with the experimental ones, as shown in Figs. 8(a) and 8(b), for $U = 2.5$ mm/s and $U = 5$ mm/s. When U was less than 10 mm/s, the experimental trajectories can be approximated by the theoretical model described by Eq. (23) for all tested liquids and sphere radii. Conversely, when U was greater than 10 mm/s, there were large discrepancies between the theoretical model and measured results as shown in Fig. 8(c). In the developed theoretical model, the initial position of the contact line, i.e., the central angle α_{CR} as shown in Fig. 7, was determined from the Laplace equation using the static advancing contact angle θ_A. However, it was observed that the actual central angle of the contact line became larger than α_{CR} as U was increased. When U is increased, the effect of dynamic wetting could not be neglected, and the model needs to include the effect of the dynamic contact angle.[28,29] The influence of the dynamic contact angle will be further discussed in Sec. IV C.

The experimental values of time at meniscus break T are shown in Fig. 9, where the solid lines represent the theoretical model result, the points represent the experimental trials, and the dashed lines represent the theoretical results in which the influence of dynamic contact angle was taken into consideration. This will be elaborated on in Sec. IV C. Under each experimental condition, T rapidly decreased from quasi-static penetration ($U = 0$) and asymptotically reached plateau as U was increased to greater than 10 mm/s. Figures 9(a) and 9(b) show the comparison of experimental results between the different contact angles for water, $\theta_A = 118°$ and $\theta_A = 155°$. T is slightly larger at $\theta_A = 155°$ than at $\theta_A = 118°$. This is because the central angle of the initial contact line position at $t = 0$ increases as the contact angle increases. Furthermore, it is intuitive that T increases as the contact line must travel a longer distance with a smaller initial velocity, as estimated by Eq. (21).

The proposed theoretical model was able to approximate the trajectory of the contact line and the rupture time of the meniscus up to $U = 10$ mm/s, and for U greater than 10 mm/s, the theoretical model tended to underestimate the rupture time. This tendency was the same for each of the experimental conditions, i.e., under varied contact angle, test liquid, and spherical radius.

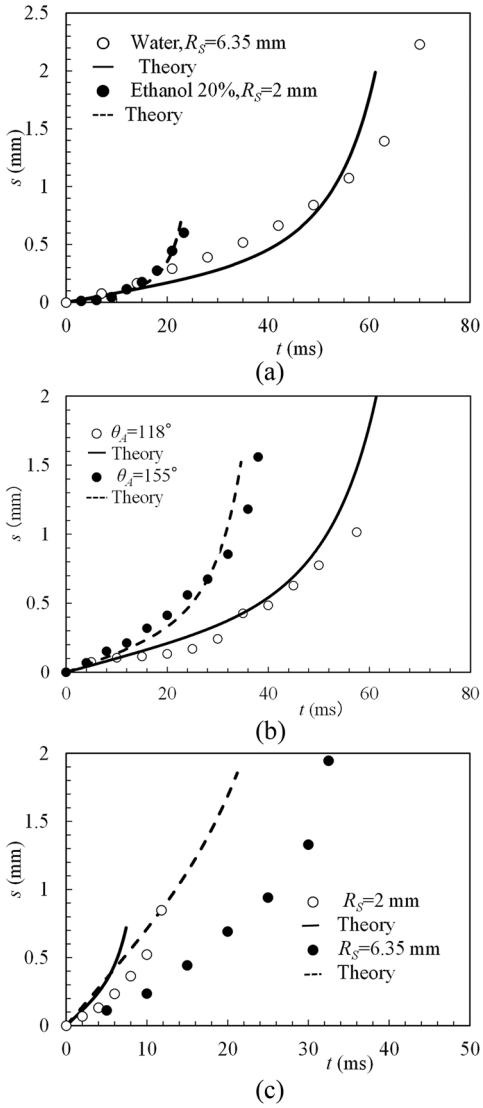

FIG. 8. Contact line trajectory. (a) $U = 2.5$ mm/s (water, $R_S = 6.35$ mm and ethanol 20% solution, $R_S = 2$ mm), (b) $U = 5$ mm/s (water, $R_S = 4$ mm: $\theta_A = 118°$ and 155°), (c) $U = 20$ mm/s (ethanol 20% solution, $R_S = 2$ mm and 6.35 mm).

B. Residual bubble volume

The experimental results for the residual bubble volume V with increasing velocity are shown in Fig. 10, where the solid lines represent the theoretical model results and the points represent the experimental trials. The dashed lines represent the theoretical results including the dynamic wetting effect which will be discussed in Sec. IV C. In all experimental conditions tested, the bubble volume gradually increased as the velocity was increased from the quasi-static state; V reaches about 1.5 to 2 times as high as that for quasi-static penetration at $U = 15$ mm/s and 2.5 to 3 times as high at $U = 25$ mm/s. As can be seen from Fig. 10(a), a change in the contact angle by 40° changed the bubble volume by one order of magnitude; the bubble volume is strongly dependent on the wettability. The influence of spherical radius R_S is shown in Fig. 10(b) for samples with a contact angle of $\theta_A = 155°$. As R_S is increased from 2 to

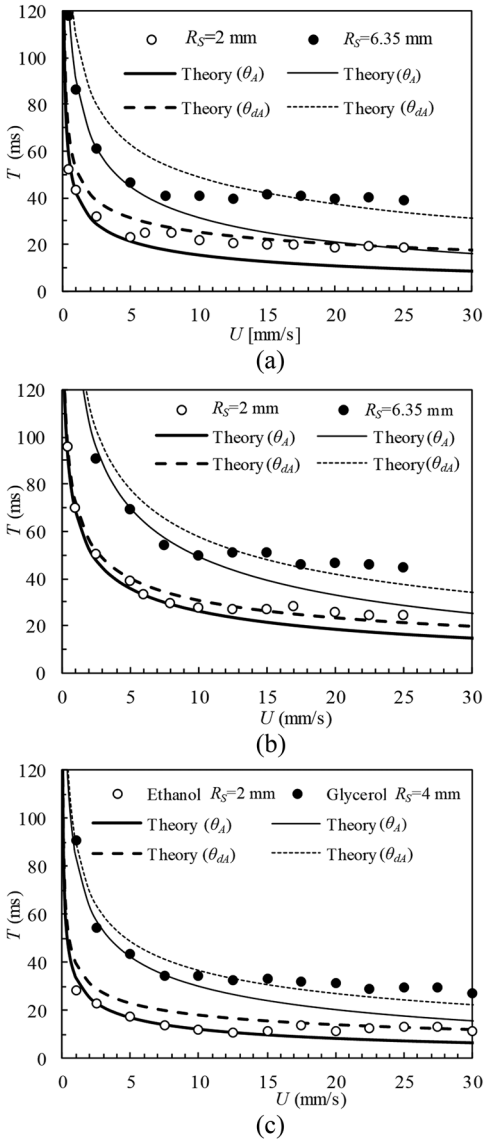

FIG. 9. Time to breakdown of meniscus. (a) Water (θ_A = 118°), (b) water (θ_A = 155°), and (c) ethanol 20% and glycerol 60% solutions.

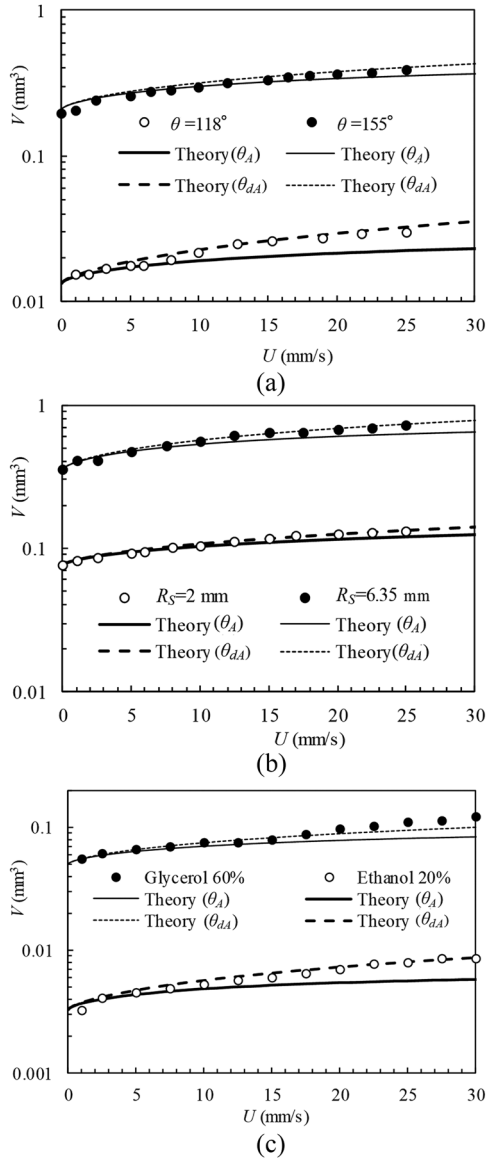

FIG. 10. Residual bubble volume. (a) Water (R_S = 4 mm), (b) water (θ = 155°, R_S = 2 mm and 6.35 mm), and (c) ethanol and glycerol solutions (R_S = 4 mm).

6.35 mm, V increases fivefold. The proposed theoretical model was again able to approximate the experimental results within an error of 10% up to U of 10 mm/s, similar to the rupture time T. As U increases greater than 10 mm/s, the experimental results tended to be increasingly larger than the calculated theoretical value for all experimental conditions tried; with U = 25 mm/s, the experimental results were between 10% and 50% larger than the theoretical value.

The deviation of the proposed theoretical model from the experimental results at high U is attributable to the deviation of the rupture time T in the experimental trials from the theoretical model. The bubble volume up to U = 10 mm/s was successfully estimated by the proposed theoretical model using the static contact angle.

C. Influence of dynamic contact angle

To better understand the influence of the dynamic contact angle, we measured the central angle α_0 of the initial contact line position. Figure 11(a) shows the results of α_0 for water and 20% aqueous ethanol. The experimental α_0 at each U was measured at t = 0, i.e., at the critical depth H_{CR} for the static advancing contact angle. Note that α_0 at U = 0 corresponds to α_{CR} for quasi-static penetration. As shown in Fig. 11(a), the initial position of the contact line deviates from that for the quasi-static U = 0 and shifts downward on the sphere surface with respect to U. Figure 11(b) shows an example of the dynamic contact angles measured at t = 0 for water with respect to the contact line velocity. The dynamic contact angle increased with increasing the velocity. The solid line shown in Fig. 11(b) represents the relation of the Hoffmann–Voinov–Tanner law to arrange the dynamic contact angle[31] as

$$\theta_{dA} = \left(\theta_A{}^3 + kCa'\right)^{1/3}, \tag{25}$$

where k is the empirical constant and Ca' is the capillary number defined using the contact line velocity. Ca' is defined as

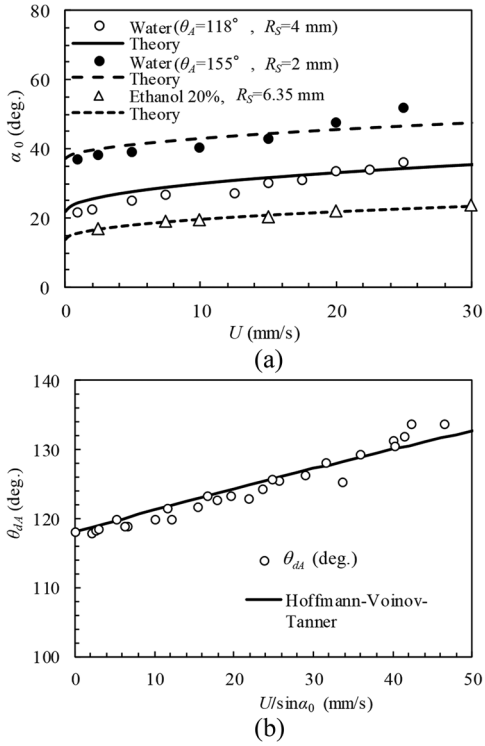

FIG. 11. (a) Center angle of the contact line at critical depth and (b) dynamic contact angle for water with Repellent 1.

$$Ca' = \frac{\rho\nu v_0}{\sigma} = \frac{\rho\nu U}{\sigma \sin \alpha_0}. \tag{26}$$

The least squares method was used to determine the corresponding k. Note that the contact line velocity v_0 in Eq. (26) was defined by using α_0 to Eq. (21) instead of α_{CR}. As shown in Fig. 11(b), we can see that the dynamic contact angle can be suitably fitted by Eq. (25). Returning to Fig. 11(a), each curve in the figure shows the central angle of the contact line position α_0 at $H = H_{CR}$ calculated by using the dynamic contact angle to Laplace equation (1). In practice, α_0 was calculated from Laplace equation (1) in which properly assumed θ_{dA} was used. Then θ_{dA} was corrected repeatedly by Newton's method to satisfy the relation of Eq. (25) in which the calculated α_0 was used to obtain the capillary number. As shown in Fig. 11(a), the final results of α_0 for the appropriate dynamic contact angle were in good agreement with the experimental results. Under the condition of $We \leq 0.1$ as targeted in this experiment, the meniscus shape can be roughly approximated by the static Laplace equation even though the contact angle was subjected to the dynamic wetting effect.

On the basis of the measurement results of the dynamic contact angle, the rupture time of the meniscus T and the bubble volume V were re-evaluated to see the effect of using the dynamic contact angle in the model. Firstly, the critical depth H_{CR}' and the central angle α_{CR}' of the contact line at H_{CR}' were obtained by applying the dynamic contact angle to the Laplace equation, shown in Eq. (1). The time ΔT for the contact line moving from quasi-static H_{CR} at $t = 0$ to H_{CR}' ($>H_{CR}$) was simply evaluated using Eq. (27)

$$\Delta T = \frac{(H_{CR}' - H_{CR})}{U}. \tag{27}$$

The trajectory after the sphere reaches H_{CR}' was recalculated by Eq. (23) in which Eq. (11) was applied to obtain the energy E_{CR}' in Eq. (13), and then the rupture time T' was calculated from Eq. (24). The total rupture time was then obtained as the sum of T' and ΔT from Eq. (27). The bubble volume V' was then obtained using the minimum energy principle at the corresponding sphere depth. The resulting T' and V' are shown by dashed lines in Figs. 9 and 10, respectively. These theoretical results show better agreement with the experimental results for both T' and V' in the range of $U > 10$ mm/s.

Figure 12 shows the percent deviation of measured bubble volumes for all experimental conditions from the theoretical model in this study with respect to the capillary number Ca defined by Eq. (28), in which U is used as the representative velocity,

$$Ca = \frac{\rho\nu U}{\sigma}. \tag{28}$$

Figures 12(a) and 12(b) show the deviation for the theoretical models using the static and dynamic contact angles, respectively. When the static contact angle was applied, the capillary numbers at which the experimental volume began to deviate by 20% from the theoretical value were 3×10^{-4} for water, 1×10^{-3} for the 20% ethanol solution, and 3×10^{-3} for the 60% glycerol solution. However, the theoretical model using

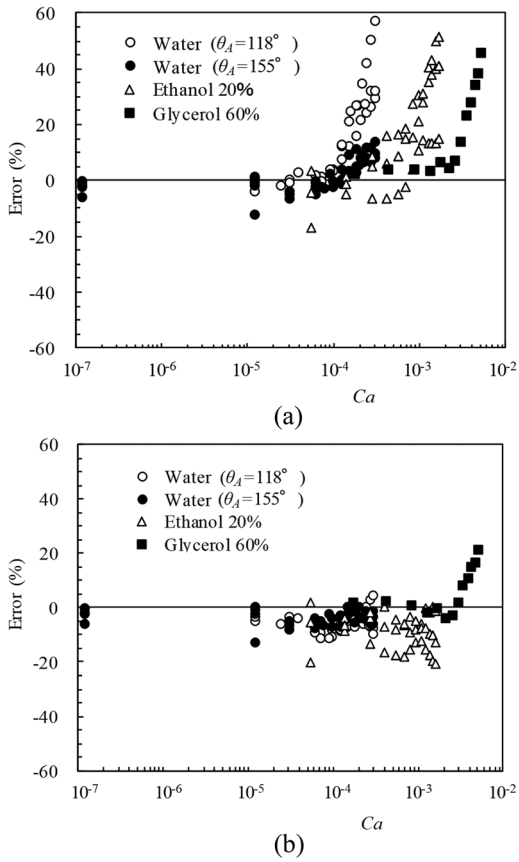

FIG. 12. Deviation of experimental bubble volumes from those obtained by the theoretical model. (a) Deviation from theory when using the static contact angle and (b) deviation from theory when using the dynamic contact angle.

the dynamic contact angle was able to evaluate almost all of the experimental bubble volumes within 20% deviation regardless of the capillary number, test liquid, contact angle, or spherical radius tested. The deviation became somewhat large for $Ca > 10^{-3}$ in the glycerol solution in Fig. 12(b). Since Ca is much smaller than unity in the experimental conditions tested, the influence of viscosity was not considered in Eq. (14) when expressing the bulk liquid motion. When the viscosity of the liquid was increased to 10 times that of water as in the glycerol solution, however, the influence of viscosity may not have been neglected. As a result, the experimental rupture time could be slightly longer, and the bubble volume was larger than the theoretical model.

Overall, the originally proposed theoretical model can predict the rupture time of the meniscus and the bubble volume for $We \sim 0.1$ in the range up to a penetration speed of 30 mm/s, as treated in this experiment.

V. SUMMARY

A theoretical model was proposed to estimate the volume of residual bubbles that adhere to spherical particles penetrating into a liquid at a finite speed. The behaviors of the contact line, the rupture time of the gas–liquid interfacial meniscus, and the volume of bubbles were determined by the proposed theoretical model and were compared with those measured in experimental trials where liquid properties, wettability, and sphere radius were varied.

An equation of motion describing the movement of the triple-phase contact line along the sphere was derived by considering the force resulted from the gradient of the system energy with respect to the contact line displacement. The calculated time trajectory of the contact line and rupture time of the meniscus roughly agreed with the experimental results for penetration speeds of less than 10 mm/s. The sphere depth at which the meniscus breaks was estimated as $H_{CR} + UT$, and the bubble volume was obtained from the principle of minimum energy. The resulting proposed theoretical model was within 10% deviation of the experimental results for penetration speeds of less than 10 mm/s.

At penetration speeds greater than 10 mm/s, the contact angle can no longer be assumed as static because of the influence of dynamic wetting behavior. Using the dynamic contact angle instead of the static contact angle at the initial position of the contact line, the rupture time and the bubble volume were calculated using the proposed theoretical model. With this change, the theoretical model could well approximate the experimental results for penetration speeds from 10 to 30 mm/s. Under the condition of $We \sim 0.1$ as studied in this experiment, it is possible to calculate the residual bubble volume by the proposed model considering the dynamic contact angle.

ACKNOWLEDGMENTS

This study was supported by JSPS KAKENHI Grant No. 15K05802. The authors are grateful to Mr. Yuki Fukui for his effort to experimental measurements.

APPENDIX: DERIVATION OF EQS. (5), (6), AND (7)

The derivations of Eqs. (5)–(7) are as follows. Figure 13 shows a reproduction of Fig. 4. δ in the figure indicates the center angle on the circular meniscus measured from the horizontal line. The volume V surrounded by the gas–liquid interface and the sphere wall can be calculated by integration as follows:

$$\begin{aligned} V &= \int_{-\beta}^{0} \pi R^3 (1 - \cos\,\delta)^2 \cos\,\delta d\delta \\ &\quad - \pi {R_S}^3 \left(\frac{1}{3}\cos^3\alpha - \cos\,\alpha + \frac{2}{3} \right) \\ &= \pi R^3 \left(\frac{1}{12}\sin\,3\beta - \frac{1}{2}\sin\,2\beta + \frac{7}{4}\sin\,\beta - \beta \right) \\ &\quad - \pi {R_S}^3 \left(\frac{1}{3}\cos^3\alpha - \cos\,\alpha + \frac{2}{3} \right). \end{aligned} \tag{A1}$$

Note that the second term on the right-hand side indicates the volume of the spherical cap with the center angle α, as shown in Fig. 13. The above result was written as Eq. (5).

The surface energy E_S of the gas–liquid interface can be obtained by multiplying the surface tension σ with the difference of surface area between the meniscus and the surface of the stationary liquid. The energy can be obtained from the following integration:

$$\begin{aligned} E_S &= \sigma \left[\int_{-\beta}^{\pi/2} 2\pi R^2 (1 - \cos\,\delta) d\delta - \pi R^2 \right] \\ &= 2\pi R^2 \sigma \left(\frac{\pi}{2} + \beta - 1 - \sin\,\beta \right) - \pi R^2 \sigma. \end{aligned} \tag{A2}$$

Finally, the potential of the liquid E_P can be estimated from the increase in the energy of the liquid displaced by the air cavity. E_P can be estimated from the following integration:

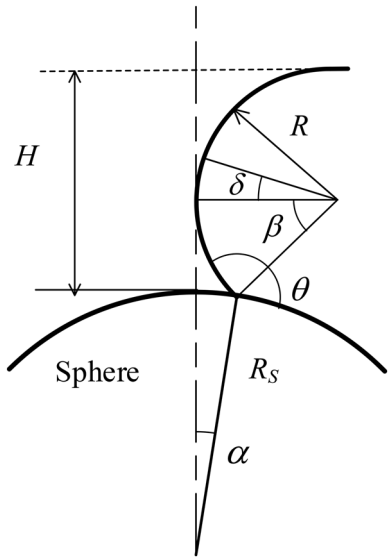

FIG. 13. Schematic of residual bubble generation (reproduced from Fig. 4).

$$
\begin{aligned}
E_P &= \rho g \int_{-\beta}^{\pi/2} \pi R^4 (1-\cos\,\delta)^2 (1-\sin\,\delta)\cos\,\delta d\delta \\
&\quad - \rho g \int_0^{\alpha} \pi {R_S}^3 \{H_{CR} + R_S(1-\cos\,\delta)\} \sin^3\,\delta d\delta. \\
&= \rho g \pi R^4 \left[\frac{5}{3} - \frac{\pi}{2} + 2\,\sin\,\beta - \frac{1}{3}\sin^3\beta - \frac{1}{2}\,\sin\,2\beta - \beta \right. \\
&\quad \left. - \frac{1}{4}\cos^4\beta + \frac{2}{3}\cos^3\beta - \frac{1}{2}\cos^2\beta \right] - \rho g \pi {R_S}^3 \\
&\quad \times \left[(H_{CR} + R_S)\left(\frac{1}{3}\cos^3\alpha - \cos\,\alpha + \frac{2}{3} \right) - \frac{1}{4} R_S \sin^4\alpha \right].
\end{aligned}
\tag{A3}
$$

The above result corresponds to Eq. (7).

[1] K. Katoh, R. Minami, T. Wakimoto, Y. Ueda, and M. Iguchi, "Residual bubble formed behind a sphere plunging into liquid bath (in Japanese)," Jpn. J. Multiphase Flow **28**, 547–553 (2015).

[2] A. M. Worthington and R. S. Cole, "Impact with a liquid surface, studied by the aid of instantaneous photography," Philos. Trans. R. Soc., A **189**, 137–148 (1897).

[3] A. M. Worthington and R. S. Cole, "Impact with a liquid surface studied by the aid of instantaneous photography. Paper II," Philos. Trans. R. Soc., A **194**, 175–199 (1900).

[4] H. Wagner, "Über stoß- und gleitvorgänge an der oberfläche von flüssigkeiten," Z. Angew. Math. Mech. **12**, 193–215 (1932).

[5] D. Gilbarg and R. A. Anderson, "Influence of atmospheric pressure on the phenomena accompanying the entry of spheres into water," J. Appl. Phys. **19**, 127–139 (1948).

[6] A. May and J. C. Woodhull, "Drag coefficients of steel spheres entering water vertically," J. Appl. Phys. **19**, 1109–1121 (1948).

[7] A. May, "Effect of surface condition of a sphere on its water-entry cavity," J. Appl. Phys. **22**, 1219–1222 (1951).

[8] A. May, "Vertical entry of missiles into water," J. Appl. Phys. **23**, 1362–1372 (1952).

[9] V. Duclaux, F. Caille, C. Duez, C. Ybert, L. Bocquet, and C. Clanet, "Dynamics of transient cavities," J. Fluid Mech. **591**, 1–19 (2007).

[10] J. M. Aristoff and J. W. M. Bush, "Water entry of small hydrophobic spheres," J. Fluid Mech. **619**, 45–78 (2009).

[11] T. T. Truscott, B. P. Epps, and A. H. Techet, "Unsteady forces on spheres during free-surface water entry," J. Fluid Mech. **704**, 173–210 (2012).

[12] C. Duez, C. Ybert, C. Clanet, and L. Bocquet, "Making a splash with water repellency," Nat. Phys. **3**, 180–183 (2007).

[13] M. Tanaka, M. Hashimoto, R. Tsujino, and M. Iguchi, "Model experiment on the hydrodynamic drag of a poorly wetted sphere penetrating into a molten metal bath," J. Jpn. Soc. Exp. Mech. **8**, 196–200 (2008).

[14] T. Tanaka, M. Hashimoto, R. Tsujino, and M. Iguchi, "Behavior of a poorly wetted low-density sphere penetrating into a water bath," J. Jpn. Soc. Exp. Mech. **8**, 201–205 (2008).

[15] Y. Ueda, M. Tanaka, T. Uemura, and M. Iguchi, "Water entry of a superhydrophobic low-density sphere," J. Visualization **13**, 289–292 (2010).

[16] D. G. Lee and H. Y. Kim, "Impact of a superhydrophobic sphere onto water," Langmuir **24**, 142–145 (2008).

[17] M. Lee, R. G. Longoria, and D. E. Wilson, "Cavity dynamics in high-speed water entry," Phys. Fluids **9**, 540–550 (1997).

[18] M. Do-Quang and G. Amberg, "The splash of a solid sphere impacting on a liquid surface: Numerical simulation of the influence of wetting," Phys. Fluids **21**, 022102 (2009).

[19] H. Ding, B. Q. Chen, H. R. Liu, C. Y. Zhang, P. Gao, and X. Y. Lu, "On the contact-line pinning in cavity formation during solid-liquid impact," J. Fluid Mech. **783**, 504–525 (2015).

[20] R. C. Hurd, J. Belden, M. A. Jandron, D. T. Fanning, A. F. Bowe, and T. T. Truscott, "Water entry of deformable spheres," J. Fluid Mech. **824**, 912 (2017).

[21] R. Bergman, D. Van Der Meer, S. Gekle, A. Van Der Bos, and D. Lohse, "Controlled impact of a disk on a water surface: Cavity dynamics," J. Fluid Mech. **633**, 381–409 (2009).

[22] T. T. Truscott, B. P. Epps, and J. Belden, "Water entry of projectiles," Annu. Rev. Fluid Mech. **46**, 355–378 (2014).

[23] B. Akers and A. Belmonte, "Impact dynamics of a solid sphere falling into a viscoelastic micellar fluid," J. Non-Newtonian Fluid Mech. **135**, 97–108 (2006).

[24] J. O. Marston, I. U. Vakarelski, and S. T. Thoroddsen, "Bubble entrapment during sphere impact onto quiescent liquid surfaces," J. Fluid Mech. **680**, 660–670 (2011).

[25] K. Sakai, T. Tokoro, and T. Hirata, "Improvement of injection desulfurization method of hot metal (in Japanese)," Tetsu to Hagane **81**, T21–T24 (1995), available at https://ci.nii.ac.jp/els/contents110001481394.pdf?id=ART0001801833.

[26] K. Katoh, "Contact angle and surface tension measurement," in *Surface and Interfacial Tension: Measurement, Theory, and Applications*, Surfactant Science Series Vol. 119, edited by S. Hartland (Marcel Dekker, 2004), pp. 375–423.

[27] S. Lahooti, O. I. Del Rio, A. W. Neumann, and P. Cheng, "Axisymmetric drop shape analysis (ADSA)," in *Applied Surface Thermodynamics*, Surfactant Science Series Vol. 63, edited by A. W. Neumann and J. K. Spelt (Marcel Dekker, 1996), pp. 441–508.

[28] Y. Yamamoto, T. Tokieda, T. Ito, T. Wakimoto, and K. Katoh, "Modeling of the dynamic wetting behavior in a capillary tube considering the macroscopic–microscopic contact angle relation and generalized Navier boundary condition," Int. J. Multiphase Flow **59**, 106–112 (2014).

[29] K. Katoh, T. Wakimoto, Y. Yamamoto, and T. Ito, "Dynamic wetting behavior of a triple-phase contact line in several experimental systems," Exp. Therm. Fluid Sci. **60**, 354–360 (2015).

[30] T. Wakimoto and K. Katoh, "Prediction of quasi-static deformation of gas-liquid interface by energy minimization principle (in Japanese)," J. Jpn. Soc. Exp. Mech. **16**, 28–35 (2016).

[31] S. F. Kistler, "Hydrodynamics of wetting," in *Wettability*, edited by J. C. Berg (Marcel Dekker, 1993), pp. 311–429.